Large Anomalous Hall Conductivity in Quasi-One-Dimensional Geometrically Frustrated Metal Pr_3MnBi_5

Xinyao Li(李鑫垚)[1,2], Feihong Guan(关飞鸿)[1,2], Xinhang Shan(闪新航)[1,2], Xiangde Zhu(朱相德)[1*], Wei Ning(宁伟)[1*], and Mingliang Tian(田明亮)[1,3,4]

[1]*Anhui Key Laboratory of Low-energy Quantum Materials and Devices, High Magnetic Field Laboratory, HFIPS, Chinese Academy of Sciences, Hefei 230031, China*
[2]*Department of Physics, University of Science and Technology of China, Hefei 230026, China*
[3]*School of Physics and Optoelectronic Engineering, Anhui University, Hefei 230601, China*
[4]*Collaborative Innovation Center of Advanced Microstructures, Nanjing University, Nanjing 210093, China*

(Received 10 November 2025; accepted manuscript online 12 February 2026)

We present the fabrication and experimental investigation of quasi-one-dimensional geometrically frustrated metal Pr_3MnBi_5 single crystals. Magnetic measurements show that the crystals exhibit two distinct ferromagnetic phase transitions at $T_{C1} = 26\,K$ and $T_{C2} = 31\,K$, accompanied by metamagnetic transitions and strong magnetic anisotropy. Large unsaturated linear positive magnetoresistance can be observed at low temperatures for different crystal orientations. Additionally, we observed a large anomalous Hall conductivity reaching up to $911\,\Omega^{-1}\cdot cm^{-1}$ in Pr_3MnBi_5, with the anomalous Hall angle reaching up to 15% at $T_{C1} = 26\,K$. These results provide valuable insights into magnetic properties and pave the way for further research into the anomalous Hall effect in geometrically low-dimensional frustrated metals.

DOI: 10.1088/0256-307X/43/4/040702 CSTR: 32039.14.0256-307X.43.4.040702

Kagome lattice materials are excellent candidates for researching quantum phenomena due to their geometric frustration.[1–3] The further incorporation of magnetic atoms into geometrically frustrated lattices provides a fertile ground for exploring magnetic order in kagome materials. For example, the $Co_3Sn_2S_2$ and AM_6X_6 families have demonstrated the feasibility of combining long-range spin interactions with the kagome lattice.[4–8] These materials exhibit magnetic and electronic instabilities that give rise to a variety of novel transport properties associated with exotic magnetic properties, such as tunable Chern gaps and anomalous Hall effects.[4–7,9] In addition to these kagome materials, another class of materials with quasi-one-dimensional (Q1D) properties provides an important platform for exploring emergent physical phenomena, such as charge density waves, superconductivity, and Luttinger liquid phases.[10–15] The coexistence of one-dimensional spin chains and interchain coupling results in long-range magnetic order being observed in Q1D magnetic materials.[11,16–18]

The R_3MX_5 (R = lanthanide; M = transition metal or Mg; X = pnictogen) materials have been identified as a promising system that combines a Q1D structure and the kagome geometrically frustrated lattice.[19–26] In these materials, MX_6 octahedral spin chains extend along the c-axis, and a distorted R-based kagome lattice is formed in the ab-plane. This combination of a low-dimensional spin chain and geometric frustration makes R_3MX_5 an excellent candidate for studying novel physical properties. For example, La_3CrAs_5 and La_3MnAs_5 undergo ferromagnetic (FM) phase transitions at 50 K and 112 K, respectively.[19,20] In contrast, Pr_3MgBi_5 exhibits an antiferromagnetic phase transition at 10.5 K, with its complex magnetic properties arising from the interplay between geometric frustration and long-range RKKY interactions.[24] Furthermore, the antiferromagnetic metal La_3MnBi_5 exhibits three phase transitions, designated $T_{N1} = 45\,K$, $T_{N2} = 42\,K$, and $T_{N3} = 24\,K$.[23] The nonmagnetic compound La_3MgBi_5 exhibits quantum oscillations and an extremely large anomalous Hall conductivity.[25,26] Additionally, SOC-induced charge-transport anisotropy has been observed in the antiferromagnetic topological material Sm_3ZrBi_5.[21,22]

In this study, we present an investigation into the Q1D geometrically frustrated metal Pr_3MnBi_5. This compound has not been studied yet, although it has a crystal structure similar to those of La_3CrAs_5, La_3MnAs_5, and La_3MnBi_5. We synthesized Pr_3MnBi_5 single crystals for the first time and performed detailed experimental measurements on both magnetic and transport properties. Temperature-dependent magnetization suggests that the compound exhibits complex magnetic properties, including two distinct FM orders and metamagnetic transitions arising from the combination of long-range magnetic order and a geometrically frustrated lattice. We found that both magnetic and transport properties exhibit strong anisotropy. At low temperatures, the crystal shows a large unsaturated positive linear magnetoresistance (MR) when

*Corresponding authors. Email: xdzhu@hmfl.ac.cn; ningwei@hmfl.ac.cn
© 2026 Chinese Physical Society and IOP Publishing Ltd. All rights, including for text and data mining, AI training, and similar technologies, are reserved.

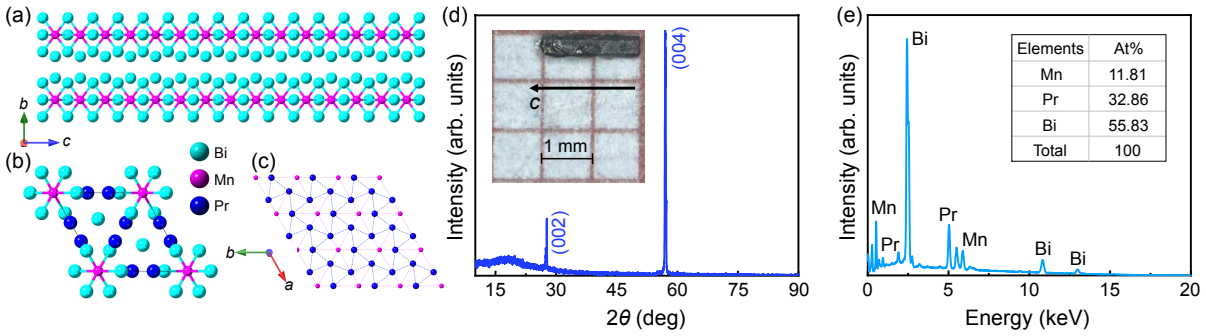

Fig. 1. (a)–(c) The crystal structure of the Pr_3MnBi_5 single crystal. (d) XRD pattern of the Pr_3MnBi_5 single crystal; the inset shows an optical photograph of a typical single crystal. (e) EDS results for the Pr_3MnBi_5 single crystal.

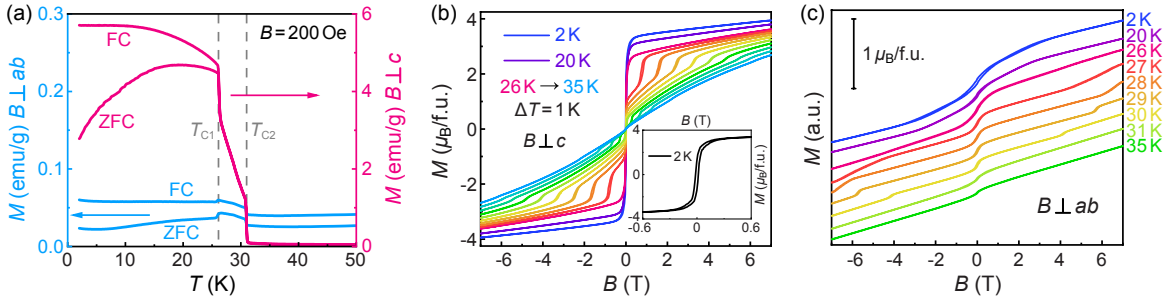

Fig. 2. (a) The temperature-dependent magnetization M curves in different directions under a magnetic field of 200 Oe. (b) and (c) The magnetic-field-dependent magnetization $M(B)$ with the field perpendicular to the c-axis and the ab plane at different temperatures, respectively.

current is applied along different crystal orientations. Furthermore, we observed a large anomalous Hall conductivity (AHC) in Pr_3MnBi_5 reaching up to 911 $\Omega^{-1}\cdot cm^{-1}$ and an anomalous Hall angle (AHA) of up to 15%. These observations provide important insights for further understanding the magnetic and physical properties of the Q1D geometrically frustrated metal Pr_3MnBi_5.

Pr_3MnBi_5 single crystals were grown using the flux method. The elemental reagents of praseodymium (99.99%), manganese (99.99%), and bismuth (99.99%) were combined at a 1:6:9 ratio in a 2 mL corundum crucible. The crucibles were then hermetically sealed in fused silica ampoules under approximately 0.5 atm of argon gas. The samples were heated to 1373 K over 10 h, held at this temperature for 15 h, and then cooled to 923 K at a rate of 3 K/h. Excess flux was removed by centrifugation at 923 K. The crystal structure of Pr_3MnBi_5 single crystals was characterized by X-ray diffraction (XRD) at room temperature using Mo Kα radiation ($\lambda = 0.71073$ Å). Electronic resistivity was measured using a Physical Property Measurement System (PPMS, Quantum Design Dynacool 14 T). Magnetic properties were measured using a Magnetic Property Measurement System (MPMS, Quantum Design 7 T).

Figures 1(a)–1(c) show the crystal structure of the Pr_3MnBi_5 single crystal. It has an anti-Hf_5Sn_3Cu hexagonal structure with space group $P6_3/mcm$ (No. 193), and its crystal structure contains a hypervalent 1D Bi chain. The $MnBi_6$ octahedra extend along the c-axis, as illustrated in Fig. 1(b). The structurally distorted kagome lattice formed by the Pr atoms, coupled with the trigonal planar coordination of the Mn atoms, establishes this material as a compelling platform for studying emergent magnetic ordering phenomena. Figure 1(d) displays the XRD pattern of the Pr_3MnBi_5 single crystal, showing preferential orientation of the $(00l)$ reflections. The inset of Fig. 1(d) shows a photograph of a Pr_3MnBi_5 single crystal, which is rod-like in shape. Figure 1(e) presents the EDS results for Pr_3MnBi_5, indicating an approximate atomic ratio of Pr:Mn:Bi of 3:1:5.

Figure 2(a) shows the temperature-dependent magnetization M versus temperature T with a magnetic field of $B = 200$ Oe applied along different directions. When the magnetic field is perpendicular to the c-axis, the $M(T)$ curve exhibits two sharp transitions at 26 K and 31 K as the temperature decreases. These transitions are defined as the FM transition temperatures T_{C1} and T_{C2}, respectively. Similar transitions are observed when the field is applied along the c-axis.

The magnetic properties of the Pr_3MnBi_5 single crystals were characterized through magnetic-field-dependent magnetization (M) measurements. Figures 2(b) and 2(c) show the isothermal magnetization data at different temperatures with the magnetic field applied perpendicular to the c-axis and the ab plane, respectively. For $B \perp c$, a typical FM behavior can be observed. Field-sweep measurements of M reveal small magnetic hysteresis. The saturation magnetization is 3.94μ_B per formula unit at 2 K. When the temperature rises above T_{C1} (~26 K), the data show a metamagnetic transition, and the critical field of the transition shifts toward higher fields. By contrast, the magnetization for $B \perp ab$ plane shows dramatic differences, as illustrated in Fig. 2(c). Strong magnetic anisotropy should be correlated with the 1D crystal structure and

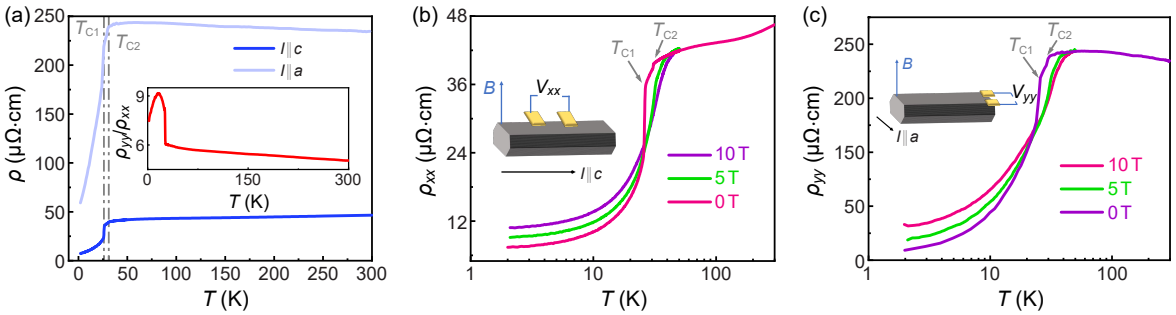

Fig. 3. (a) The temperature dependence of resistivity ρ for different current directions. The inset shows the ratio between ρ_{yy} and ρ_{xx}. (b) and (c) The temperature dependence of ρ_{xx} and ρ_{yy} under different magnetic fields. The insets in (b) and (c) show the configurations of the magnetic field, electric current, and voltage lead directions in the measurements.

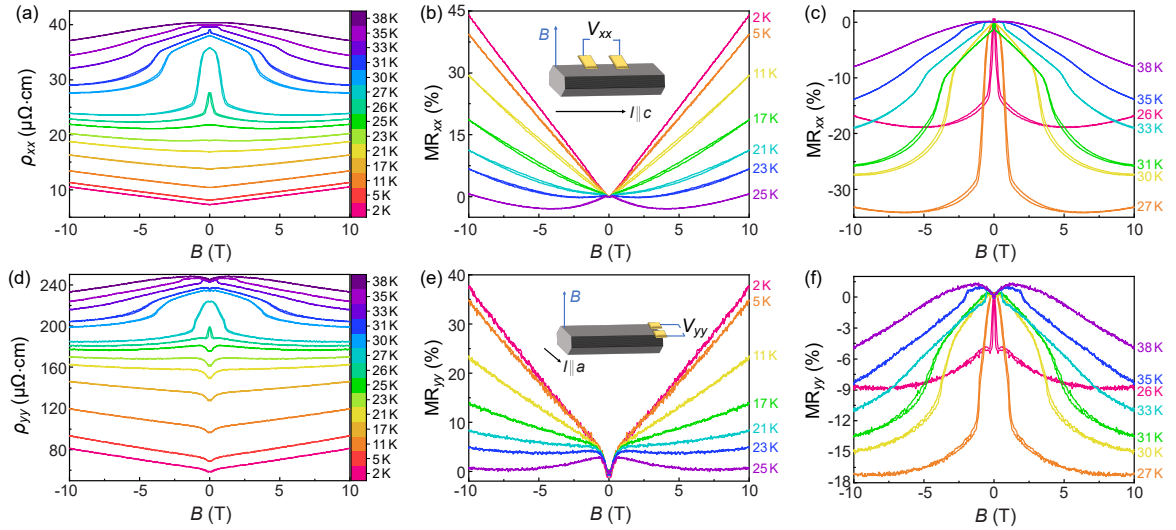

Fig. 4. (a) The magnetic-field-dependent resistivity at different temperatures with $I \| c$ and $B \perp c$. (b) and (c) The MR curves at different temperatures with $I \| c$ and $B \perp c$. (d) The magnetic-field-dependent resistivity at different temperatures with $I \| a$ and $B \perp c$. (e) and (f) The MR curves at different temperatures with $I \| a$ and $B \perp c$.

the long-range magnetic order. However, the observed magnetization is considerably weaker, with a magnetization value of approximately 0.06 emu/g under a magnetic field of 7 T ($M_{B\perp c}/M_{B\perp ab} \sim 95$), indicating a significant degree of magnetic anisotropy.

Figure 3 shows the temperature-dependent resistivity ρ curves, which were measured with current applied along different crystal orientations. The configurations of the electric current and voltage lead directions are shown in the insets of Figs. 3(b) and 3(c). The subscript xx (yy) stands for $I \| c$ ($I \| a$). Figure 3(a) shows that both curves exhibit metallic behavior, with two FM phase transitions occurring at $T_{C1} = 26$ K and $T_{C2} = 31$ K. The curves also demonstrate pronounced resistivity anisotropy under different current directions. The temperature dependence of resistivity anisotropy ρ_{yy}/ρ_{xx} is plotted in the inset of Fig. 3(a). Large resistivity anisotropy can be observed, with a maximum ratio ρ_{yy}/ρ_{xx} over 9 at $T_{C1} = 26$ K. Figures 3(b) and 3(c) show the ρ_{xx} and ρ_{yy} curves measured under different magnetic fields. As the magnetic field increases, the two FM phase transitions shift toward higher temperatures and are ultimately suppressed above 10 T.

Figure 4 shows the MR, defined as MR $= \{[R(B) - R(0)]/R(0)\} \times 100\%$, with the current and magnetic field applied in different directions. The magnetic field dependence of the resistivity (ρ_{xx} and ρ_{yy}) curves is shown in Figs. 4(a) and 4(d). At low temperatures, the MR is positively saturated, i.e., reaches 44% at 2 K under a magnetic field of 10 T with $I \| c$ and $B \perp c$. Upon increasing the temperature, the MR curves display slight hysteresis, which is likely related to magnetization hysteresis. As the temperature approaches the first FM ordering temperature ($T_{C1} \sim 26$ K), the positive MR transitions to negative behavior. Further increasing the temperature to above T_{C1} results in a cusp-shaped negative MR, as shown in Fig. 4(c). The negative MR in Pr_3MnBi_5 should be attributed to the suppression of spin order under magnetic field, a phenomenon commonly observed in magnetic systems.[27] At $T = 27$ K, the negative MR reaches a maximum value of approximately -34.2% at $B \sim 6$ T with $I \| c$ and $B \perp c$. When the temperature approaches the second FM ordering temperature ($T_{C2} \sim 31$ K), a distinct cusp-shaped negative MR emerges. As the temperature increases further, the cusp-shaped negative MR evolves into a platform shape, and the metamagnetic transition following the cusp-shaped MR becomes less pronounced. The temperature dependence of MR should be related to the complex magnetization transition driven by thermal

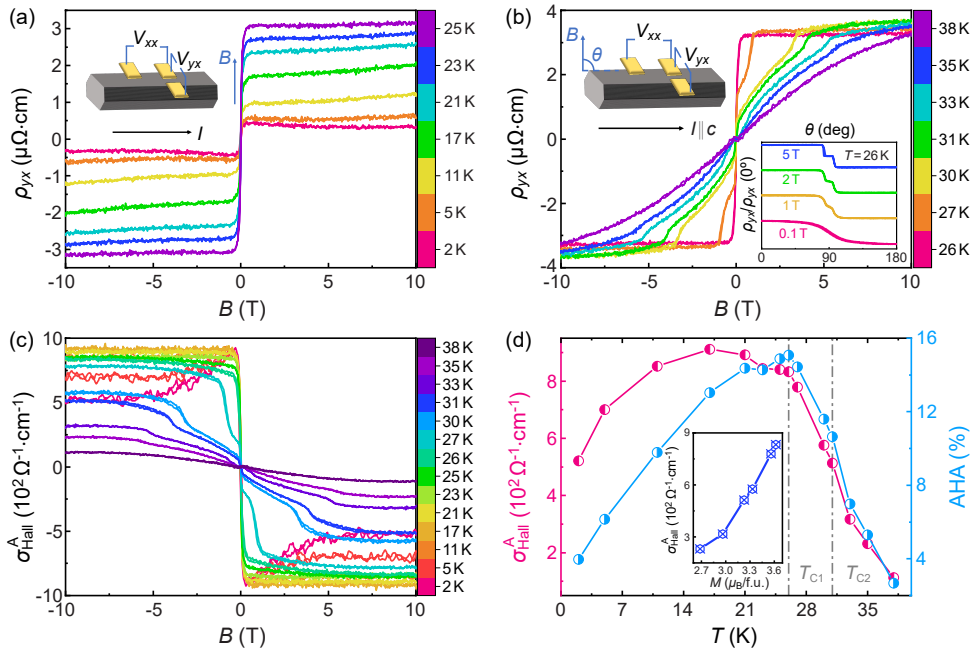

Fig. 5. (a) and (b) The ρ_{yx} at different temperatures from 2 K to 38 K with current applied along the c-axis. The inset of (b) shows the angular-dependent ρ_{yx} and the configuration of the magnetic field and current in angular-dependent measurements. (c) The AHC at different temperatures from 2 K to 38 K. (d) The temperature dependence of AHC and AHA. The inset shows the relationship between AHC and magnetization above $T_{C1} = 26$ K.

effects.[27–29] Furthermore, the MR_{yy} curves in Figs. 4(e) and 4(f) exhibit similar behavior to that of the MR_{xx} curves in Figs. 4(b) and 4(c) under different current configurations in the transport measurements. Figure 4(e) shows a similarly unsaturated linear positive MR up to 37.6% at 2 K in a 10 T magnetic field. As temperature increases, the MR_{yy} curve exhibits a similar metamagnetic transition and negative MR behavior. The negative MR reaches a maximum value of approximately −17.2% at $T = 27$ K, as shown in Fig. 4(f). This indicates that the Q1D structure influences the carrier transport behavior without altering the magnetic properties of the single crystal.

We further performed Hall resistivity ρ_{yx} measurements on Pr_3MnBi_5 single crystals at different temperatures. Figures 5(a) and 5(b) present the dependence of ρ_{xy} on magnetic field at temperatures below T_{C1} and between T_{C1} and T_{C2}, respectively. The inset schematic of Fig. 5(a) shows the configuration of the magnetic field, electric current, and voltage lead directions in Hall resistivity measurements. In general, ρ_{yx} of a FM conductor can be described by the expression $\rho_{yx} = R_H B + 4\pi R_S M$, where $R_H B$ represents the ordinary Hall contribution due to the Lorentz effect (R_H: Hall coefficient) and $4\pi R_S M$ is the anomalous Hall contribution. As shown in Figs. 5(a) and 5(b), ρ_{yx} shows a similar magnetic field dependence as the isothermal magnetization presented in Fig. 2(b), suggesting that the anomalous Hall contribution (proportional to M) is dominant. The ordinary Hall contribution was found to be relatively small, accounting for only 0.9%–2.7% of the total ρ_{yx} over the field range of 0.5–10 T, where M is saturated. We extracted the mobility and carrier density by subtracting the AHE contribution. The results show that hole-type carriers dominate the transport process. The largest mobility value $\mu_p \sim 196.9\,cm^2{\cdot}V^{-1}{\cdot}s^{-1}$ can be observed at $T_{C1} = 26$ K, while the concentration (n_p) in Pr_3MnBi_5 single crystals is close to $10^{22}\,cm^{-3}$ at $T = 2$ K. As the temperature increases, n_p gradually decreases and μ_p increases, attaining a maximum value of $196.9\,cm^2{\cdot}V^{-1}{\cdot}s^{-1}$ at $T_{C1} = 26$ K. Due to the strong magnetic anisotropy in Pr_3MnBi_5 single crystals, we performed angular-dependent ρ_{yx} measurements with the current applied along the c-axis. The inset of Fig. 5(b) shows the configuration of the angular-dependent ρ_{yx} measurements under different magnetic fields at the first FM ordering transition ($T_{C1} \sim 26$ K).

Due to the pronounced resistivity anisotropy in the Q1D material [see Fig. 3(a)], the Hall conductivity of the Pr_3MnBi_5 single crystal can be defined as $\sigma_{Hall} = -\rho_{yx}/(\rho_{xx}\rho_{yy} + \rho_{yx}^2)$. The obtained results are shown in Figs. 5(c) and 5(d). The value of AHC is as large as about $911\,\Omega^{-1}{\cdot}cm^{-1}$ at $T = 17$ K. With increasing temperature, the AHC decreases gradually and remains up to $113\,\Omega^{-1}{\cdot}cm^{-1}$ at $T = 38$ K. Besides the large AHC, Pr_3MnBi_5 also exhibits a large AHA, $\Theta_H = \sigma^A_{Hall}/\sigma_{xx}$, as shown in Fig. 5(d). The AHA increases gradually with increasing temperature, reaching a large value of 15% at $T_{C1} = 26$ K, and then decreases gradually as the temperature further increases. In addition, we observed that above $T_{C1} = 26$ K, both the AHC and the saturation magnetization decrease with increasing temperature, as shown in the inset of Fig. 5(d). This suggests that the magnetic ion moments and spin configurations influence the carrier transport behavior, thereby altering the transport properties. Similar behavior has been observed in previous research on the Weyl semimetal $Co_3Sn_2S_2$.[5]

AHC usually measures the total contributions from

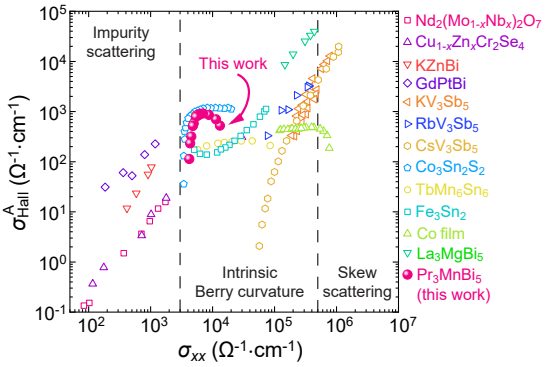

Fig. 6. Map of AHC for various materials and logarithmic plot of AHC versus σ_{xx}. The AHC of Pr_3MnBi_5 (solid pink dot) exhibits a complex nonlinear relationship with σ_{xx}.

various intrinsic and extrinsic mechanisms. Extrinsic contributions result from side jumps and skew scattering, while intrinsic contributions are theoretically determined from electronic band structures. The scaling relation between AHC and σ_{xx} is widely used to extract the contributions from intrinsic and extrinsic mechanisms. We have performed a similar scaling analysis, as shown in Fig. 6. By comparing it with several typical materials that exhibit large AHC,[6,26,30–32] we found that Pr_3MnBi_5 exhibits a complex nonlinear relationship between AHC and σ_{xx}, suggesting that the AHE in Pr_3MnBi_5 involves a complex and variable hybrid mechanism.[33] This phenomenon may originate from the evolution of the band structure and the spin configurations of the magnetically geometrically frustrated sublattice at different temperatures.

In conclusion, we successfully fabricated the Q1D, geometrically frustrated metal Pr_3MnBi_5 and performed detailed magnetic and magneto transport measurements. The crystal exhibits two distinct FM orders at $T_{C1} = 26$ K and $T_{C2} = 31$ K, and a metamagnetic transition and magnetic anisotropy are evident in both MR and $M(B)$ curves. Meanwhile, transport measurements revealed pronounced resistivity anisotropy under different crystal orientations. The MR curves show a large unsaturated linear positive MR at low temperatures for different current and magnetic field directions. Furthermore, we observed a large AHC of up to 911 Ω^{-1}·cm^{-1} at $T = 17$ K and an AHA of up to 15% at $T_{C1} = 26$ K, which may indicate a complex and variable hybrid mechanism due to the complex nonlinear relationship between AHC and σ_{xx}. Further investigation combining neutron diffraction and theoretical calculations may help reveal the detailed spin configuration and band structure, and thus elucidate the mechanism of the AHE in Pr_3MnBi_5. These findings provide useful information for understanding the magnetic properties and nontrivial topological physics in the Q1D, geometrically frustrated metal Pr_3MnBi_5.

Acknowledgements. This work was supported by the National Key Research and Development Program of China (Grant No. 2023YFA1607400), the Natural Natural Science Foundation of China (Grant No. 12474052), the HFIPS Director's Fund (Grant No. YZJJQY202304), the Youth Innovation Promotion Association of the Chinese Academy of Sciences (Grant No. 2021117), the Natural Science Foundation of Anhui Province (Grant No. 1908085QA15), and the Anhui Provincial Major S&T Project (Grant No. s202305a12020005). A portion of this work was supported by the Basic Research Program of the Chinese Academy of Sciences Based on Major Scientific Infrastructures (Grant No. JZHKYPT-2021-0), the High Magnetic Field Laboratory of Anhui Province (Contract No. AHHM-FX-2020-02).

References

[1] Majumder M, Gupta R, Luetkens H, Khasanov R, Stockert O, Gegenwart P, and Fritsch V 2022 *Phys. Rev. B* **105** L180402
[2] Wang W, Li Z, Xiang Y, and Wang Q 2013 *Phys. Rev. B* **87** 115135
[3] Kang M, Ye L, Fang S, You J, Levitan A, Han M, Facio J I, Jozwiak C, Bostwick A, Rotenberg E, Chan M, McDonald R D, Graf D, Kaznatcheev K, Vescovo E, Bell D C, Kaxiras E, van den Brink J, Richter M, Prasad G M, Checkelsky J G, and Comin R 2020 *Nat. Mater.* **19** 163
[4] Liu E, Sun Y, Kumar N, Muchler L, Sun A, Jiao L, Yang S, Liu D, Liang A, Xu Q, Kroder J, Suss V, Borrmann H, Shekhar C, Wang Z, Xi C, Wang W, Schnelle W, Wirth S, Chen Y, Goennenwein S T B, and Felser C 2018 *Nat. Phys.* **14** 1125
[5] Wang Q, Xu Y, Lou R, Liu Z, Li M, Huang Y, Shen D, Weng H, Wang S, and Lei H 2018 *Nat. Commun.* **9** 3681
[6] Gao L, Shen S, Wang Q, Shi W, Zhao Y, Li C, Cao W, Pei C, Ge J, Li G, Li J, Chen Y, Yan S, and Qi Y 2021 *Appl. Phys. Lett.* **119** 092405
[7] Ma W, Xu X, Yin J, Yang H, Zhou H, Cheng Z, Huang Y, Qu Z, Wang F, Hasan M Z, and Jia S 2021 *Phys. Rev. Lett.* **126** 246602
[8] Li L, Chi S, Ma W, Guo K, Xu G, and Jia S 2024 *Chin. Phys. B* **33** 057501
[9] Pokharel G, Ortiz B R, Chamorro J, Sarte P M, Kautzsch L, Wu G, Ruff J, and Wilson S D 2022 *Phys. Rev. Mater.* **6** 104202
[10] Denholme S J, Yukawa A, Tsumura K, Nagao M, Tamura R, Watauchi S, Tanaka I, Takayanagi H, and Miyakawa N 2017 *Sci. Rep.* **7** 45217
[11] Liu Z, Dong Q, Yang P, Shan P, Wang B, Sun J, Dun Z, Uwatoko Y, Chen G, Dong X, Zhao Z, and Cheng J 2022 *Phys. Rev. Lett.* **128** 187001
[12] Mu Q, Ruan B, Pan B, Liu T, Yu J, Zhao K, Chen G, and Ren Z 2017 *Phys. Rev. B* **96** 140504
[13] Islam S S, Mukharjee P K, Biswas P K, Telling M, Skourski Y, Ranjith K M, Baenitz M, Inagaki Y, Furukawa Y, Tsirlin A A, and Nath R 2024 *Phys. Rev. B* **109** L060406
[14] Zhao K, Mu Q, Ruan B, Zhou M, Yang Q, Liu T, Pan B, Zhang S, Chen G, and Ren Z 2020 *Chin. Phys. Lett.* **37** 097401
[15] Zhou Y, Chen L, Wang G, Wang Y, Wang Z, Chai C, Guo Z, Hu J, and Chen X 2022 *Chin. Phys. Lett.* **39** 047401
[16] de Jongh L J 1978 *J. Appl. Phys.* **49** 1305
[17] Chen L, Zhao L, Qiu X, Zhang Q, Liu K, Lin Q, and Wang G 2021 *Inorg. Chem.* **60** 12941
[18] Bao J, Tang Z, Jung H, Liu J, Liu Y, Li L, Li Y, Xu Z, Feng C, Chen H, Chung D, Dravid V P, Cao G, and Kanatzidis M G 2018 *J. Am. Chem. Soc.* **140** 4391
[19] Duan L, Wang X, Zhang J, Zhao J, Zhao Z, Xiao C, Guan C, Wang S, Shi L, Zhu J, and Jin C 2022 *J. Alloy. Compd.* **905** 164214

[20] Duan L, Wang X, Zhang J, Hu Z, Zhao J, Feng Y, Zhang H, Lin H, Chen C, Wu W, Li Z, Wang R, Zhang J, Xiang T, and Jin C 2022 *Phys. Rev. B* **106** 184405
[21] Khoury J F, Han B, Jovanovic M, Queiroz R, Yang X, Singha R, Salters T H, Pollak C J, Lee S B, Ong N P, and Schoop L M 2024 *Adv. Mater.* **36** 2404553
[22] Khoury J F, Han B, Jovanovic M, Singha R, Song X, Queiroz R, Ong N P, and Schoop L M 2024 *J. Am. Chem. Soc.* **144** 9785
[23] Zhang C, Wang Y, Zheng J, Du L, Li Y, Han X, Liu E, Wu Q, and Shi Y 2024 *Phys. Rev. Mater.* **8** 034402
[24] Han X, Li Y, Yang M, Miao S, Yan D, and Shi Y 2023 *Phys. Rev. Mater.* **7** 124406
[25] Han X, Pi H, Yan D, Zhang R, Li Y, Wang X, Dun Z, Wang Z, Feng H, Wu Q, and Shi Y 2023 *Phys. Rev. B* **108** 075157
[26] Yi Z, Ouyang Z, Guo P, Liang H, Li Y, Su P, Li N, Zhou Y, Wu D, Sun Y, Yue X, Li Q, Wang S, Sun X, and Wang Y 2024 *Adv. Mater.* **36** e2400166
[27] Shi G, Zhang M, Yan D, Feng H, Yang M, Shi Y, and Li Y 2020 *Chin. Phys. Lett.* **37** 047301
[28] Chen H, Lou Z, Zhou Y, Chen Q, Xu B, Chen S, Du J, Yang J, Wang H, and Fang M 2020 *Chin. Phys. Lett.* **37** 047201
[29] Majumder C, Bhattacharya S, and Saha S K 2020 *J. Magn. Magn. Mater.* **506** 166601
[30] Wang Y, Chen Z, Nie Y, Zhang Y, Niu Q, Zheng G, Zhu X, Ning W, and Tian M 2023 *Phys. Rev. B* **108** 035117
[31] Yang S, Wang Y, Ortiz B R, Liu D, Gayles J, Derunova E, Gonzalez-Hernandez R, Smejkal L, Chen Y, Parkin S S P, Wilson S D, Toberer E S, McQueen T M, and Ali M N 2020 *Sci. Adv.* **6** eabb6003
[32] Yu F, Wu T, Wang Z, Lei B, Zhuo W, Ying J, and Chen X 2021 *Phys. Rev. B* **104** L041103
[33] Roychowdhury S, Samanta K, Singh S, Schnelle W, Zhang Y, Noky J, Vergniory M G, Shekhar C, and Felser C 2024 *Proc. Natl. Acad. Sci. U. S. A.* **121** e2401970121